Dynamical response and competing orders in two-band Hubbard model

A. Niyazi [1], D. Geffroy [2,1] and J. Kuneš [1,3]

[1]*Institute of Solid State Physics, TU Wien, 1040 Vienna, Austria*

[2]*Department of Condensed Matter Physics, Faculty of Science, Masaryk University, Kotlářská 2, 611 37 Brno, Czechia*

[3]*Institute of Physics, Czech Academy of Sciences, Na Slovance 2, 182 21 Praha 8, Czechia*

(Received 17 June 2020; accepted 6 August 2020; published 31 August 2020)

We present a dynamical mean-field study of two-particle dynamical response functions in a two-band Hubbard model across several phase transitions. We observe that the transition between the excitonic condensate and spin-state ordered state is continuous with a narrow strip of supersolid phase separating the two. Approaching transition from the excitonic condensate is announced by softening of the excitonic mode at the M point of the Brillouin zone. Inside the spin-state ordered phase there is a magnetically ordered state with 2×2 periodicity, which has no precursor in the normal phase.

DOI: 10.1103/PhysRevB.102.085159

I. INTRODUCTION

Spontaneous symmetry breaking, which accompanies the continuous phase transitions, changes qualitatively the dynamical response of solids. If the broken symmetry is continuous, low-energy Goldstone mode(s) associated with the long-wavelength dynamics of the order parameter, appears in systems with short-range interactions. Excitonic condensates (ECs) [1–3] represent an exotic type of broken-symmetry phase. While the experimental realizations of EC have been limited to artificial structures such as quantum wells in strong magnetic field [4] or cavity systems [5], recent experiments on 1T-$TiSe_2$ [6,7], Ca_2RuO_4 [8] or $Pr_{0.5}Ca_{0.5}CoO_3$ [9,10] revived interest in the subject also in bulk solids. Condensation of spinful excitons, which gives rise to a new type of magnetic behavior is particularly interesting. The simplest model to capture the excitonic magnetism is the two-orbital Hubbard model at half filling [11–13] and its strong-coupling limit [14–16]. The parameter range of interest hosts a number of ordered phases [15,17] in addition to the first-order metal-insulator transition [18]. Besides the general interest in understanding its behavior, the model provides a fertile playground for testing theoretical methods.

Computation of two-particle (2P) response for realistic materials is a challenging task. Dynamical mean-field theory (DMFT) [19,20] has been successful in bringing together the material realism of multi-orbital models with the many-body realism, including real temperatures, phase transitions, quasiparticle life times, atomic-multiplet effects. Despite the boom of the past two decades, application of DMFT has been largely limited to one-particle (1P) quantities, such as generalized band structures and occupation numbers. Solved in principle, the calculation of 2P response functions is numerically very demanding as it involves the solution of the Bethe-Salpeter equation for large multi-index objects. There are compelling reasons to study the 2P response within DMFT. Most experimental probes and applications employ the 2P response of materials. Current density functional methods do not allow even approximate access to dynamical susceptibilities of correlated materials. The static susceptibilities are essential to ensure the stability of the obtained solutions.

In this paper we study the dynamical susceptibilities of the two-orbital Hubbard model on a bipartite lattice at half filling. In particular, we focus on the mechanism of transition between the EC and spin-state order (SSO) phases. The studied phase transitions involve both continuous and discrete symmetry breaking and multi-atomic unit cells. Besides understanding the physics of the model and assessing the performance of the method, this work is the next step towards similar investigations within the local density approximation (LDA)+DMFT framework for real materials.

II. COMPUTATIONAL METHOD

The studied model Hamiltonian reads

$$\begin{aligned} H = & \sum_{\langle ij\rangle,\sigma} (t_a a^\dagger_{i\sigma} a_{j\sigma} + t_b b^\dagger_{i\sigma} b_{j\sigma}) + \text{H.c} \\ & + \frac{\Delta}{2} \sum_{i,\sigma} \left(n^a_{i\sigma} - n^b_{i\sigma}\right) \\ & + U \sum_{i,c=a,b} n^c_{i\uparrow} n^c_{i\downarrow} + \sum_{i,\sigma\sigma'} (U' - J\delta_{\sigma\sigma'}) n^a_{i\sigma} n^b_{i\sigma'}, \end{aligned} \quad (1)$$

where $a^\dagger_{i\sigma}$ and $b^\dagger_{i\sigma}$ are the fermionic creation operators for electrons in the respective orbitals a and b, with spin σ, at site i of a square lattice. The first term describes nearest neighbor hopping. The remaining terms, containing the particle number operators $n^c_{i,\sigma} \equiv c^\dagger_{i\sigma} c_{i\sigma}$, correspond to the crystal-field Δ, the Hubbard interaction U, and Hund's exchange J in the Ising approximation. The values $U = 4$, $J = 1$, and $U' = U - 2J$ are fixed throughout this study. The remaining parameters t_a, t_b, Δ as well as the temperature T are varied. The hopping amplitudes, chosen to include those of Refs. [21,22], are

varied so that the sum $t_a^2 + t_b^2 = 0.205$ is fixed. We use the ratio $\xi = \frac{2t_a t_b}{t_a^2+t_b^2}$ to characterize the difference between the a and b bandwidth ($\xi = 1$ equal bandwidths, $\xi = 0$ one band is flat). This choice is motivated by the strong-coupling limit, in which $t_a^2 + t_b^2$ determines the repulsion between excitons on neighbor sites, while $t_a t_b$ determines the amplitude of exciton hopping [17]. Smaller ξ thus favors the SSO phase, while larger ξ favors the EC phase. All calculations reported here are performed for the filling of two electrons per atom.

We follow the standard DMFT procedure, in which the lattice model is mapped onto an auxiliary Anderson impurity model (AIM) [23,24]. The auxiliary model is solved numerically, using the ALPS implementation [25–27] of the matrix version of the strong-coupling continuous-time quantum Monte-Carlo (CT-QMC) algorithm [28].

The model hosts several competing phases, which can be distinguished by the mean values of operators

$$\begin{aligned} \phi_i^\gamma &= R_i^\gamma + iI_i^\gamma = \sum_{\alpha\beta} \sigma_{\alpha\beta}^\gamma a_{i\alpha}^\dagger b_{i\beta}, \\ O_i &= \sum_\sigma \left(n_{i\sigma}^a - n_{i\sigma}^b\right), \\ S_i^z &= \sum_{c=a,b} \left(n_{i\uparrow}^c - n_{i\downarrow}^c\right). \end{aligned} \tag{2}$$

Here ϕ_i^γ, with the Hermitean and anti-Hermitean parts R_i^γ and iI_i^γ, creates an $S = 1$ exciton on site i. The σ^γ ($\gamma = x, y, z$) are Pauli matrices, which represent the spin polarization of the exciton. With the density-density form of the interaction, which mimics an easy-axis single-ion anisotropy, $\langle \phi_i^z \rangle = 0$ applies throughout the studied parameter range [17]. The O_i and S_i^z represent the local orbital polarization and the z component of the spin moment, respectively.

The susceptibilities $\chi^X(\mathbf{k}, \omega)$ are obtained by analytic continuation [29,30] of their Matsubara representations

$$\chi^X(\mathbf{k}, i\nu_n) = \int_0^\beta \mathrm{d}\tau e^{i\nu_n \tau} \langle X_{-\mathbf{k}}(\tau) X_{\mathbf{k}}(0) \rangle - |\langle X_{\mathbf{k}} \rangle|^2, \tag{3}$$

where the Fourier transform is defined as $X_{\mathbf{k}} = \frac{1}{\sqrt{N}} \sum_{\mathbf{R}} e^{-i\mathbf{k}\cdot\mathbf{R}} X_{\mathbf{R}}$. The observables X of interest are represented by the operators listed in Eq. (2).

We start with the 1P propagators at 300 Matsubara frequencies to obtain the bare susceptibilities (both local and lattice bubble terms), which are then transformed into the Legendre polynomial representation [31]. The 2P correlation function is sampled using the CT-QMC algorithm. The local 2P-irreducible vertex Γ is obtained by inverting the impurity Bethe-Salpeter equation (BSE) [19,32–34]. Using this vertex to solve the lattice BSE, we obtain the lattice correlation functions. This procedure is performed independently for each bosonic Matsubara frequency. We have found that using 10 bosonic frequencies allows for a stable and good quality analytic continuation. We use between 22 (for the zeroth bosonic frequency) and 30 Legendre coefficients (for the ninth bosonic frequency). A sizable reduction of the computational and storage cost can be achieved with the procedure of Refs. [35,36].

The susceptibility $\chi^X(\mathbf{k}, i\nu_n)$ is a diagonal element of the particle-hole susceptibility matrix $\boldsymbol{\chi}(\mathbf{k}, i\nu_n)$ obtained by summation of the lattice correlation function over the Legendre coefficients. The matrix $\boldsymbol{\chi}(\mathbf{k}, i\nu_n)$ is indexed by pairs of flavors (spin/orbital/site) inside the unit cell, while the intercell structure is diagonalized by going to the reciprocal space. With four flavors per site, $\boldsymbol{\chi}(\mathbf{k}, i\nu_n)$ has dimension 4^2 for a one-atom cell. In phases with two-atom cells $\boldsymbol{\chi}(\mathbf{k}, i\nu_n)$ has the dimension $(2 \times 4)^2$. However, thanks to the locality of the 2P-irreducible vertices, the BSE can be written in a closed form for elements of the type $\chi_{ii,jj}$, where i, j are the site indices. Therefore the diagonal elements in (3) can be obtained by working with matrices of the flavor dimension 2×4^2, i.e., linear in the number of sites per the unit cell.

To ensure comparability of $\chi^X(\mathbf{k}, i\nu_n)$ in different phases (various unit cells) we present all susceptibilities (3) in the large Brillouin zone of the one-atom unit cell. In the phases with one-atom unit cell the susceptibility is diagonal in $\mathbf{k}$. In phases with $\sqrt{2} \times \sqrt{2}$ two-atom unit cells there are nonzero off-diagonal elements connecting $\mathbf{k}$ and $\mathbf{k} + (\pi, \pi)$. The transformation from the two-atom unit cell, in which the BSE inversion is performed, is given by

$$\begin{aligned} \chi(\mathbf{k}) = \tilde{\chi}(\mathbf{k}')_{11,11} + \tilde{\chi}(\mathbf{k}')_{22,22} \\ + \exp(ik_y)\tilde{\chi}(\mathbf{k}')_{11,22} + \exp(-ik_y)\tilde{\chi}(\mathbf{k}')_{22,11}, \end{aligned} \tag{4}$$

where $\tilde{\chi}$ and $\mathbf{k}' \equiv (k'_x, k'_y) = (k_y - k_x, k_y + k_x)$ are related to the two-atom unit cell. The subscripts of $\tilde{\chi}$ refer to the two sites in the two-atom unit cell (The orbital and spin indices are not shown for sake of simplicity).

III. RESULTS AND DISCUSSION

A. Phase diagram and order parameters

Four distinct ordered phases, shown in Fig. 1 and discussed below, have been identified. In Fig. 2 we show the phase diagram of the model in the ξ–T plane of band asymmetry parameter $\xi = \frac{2t_a t_b}{t_a^2+t_b^2}$ and temperature T at fixed crystal field Δ, and in the Δ–T plane at fixed ξ. The phase boundaries are obtained by combination of the calculated order parameters and diverging susceptibilities. The phase diagram in Fig. 2(a) generalizes that of Ref. [21] to the ordered phases. The phase diagram in Fig. 2(b) should be compared to the phase diagrams of related strong-coupling models in Refs. [16,17]. Unlike previous studies [12,21] where the instabilities of the normal phase were investigated, here we perform linear response calculations also in the thermodynamically stable ordered phases.

Polar excitonic condensate. This phase was analyzed in detail in a number of previous studies [13,15,37–39]. It is characterized by a finite expectation value of $\langle \boldsymbol{\phi}_i \rangle = \boldsymbol{\phi}$, which fulfills the condition $\boldsymbol{\phi}^* \times \boldsymbol{\phi} = 0$ [39,40]. The EC phase preserves the translation symmetry, but breaks two continuous $U(1)$ symmetries associated with the global conservation of $\sum_i S_i^z$ and $\sum_i O_i$. The EC order parameter lives on a T_2 torus; it can pick an arbitrary orientation in the spin xy plane and an arbitrary complex phase. Throughout the present study we fix its orientation to $\langle I^y \rangle \neq 0$, while the other components are zero.

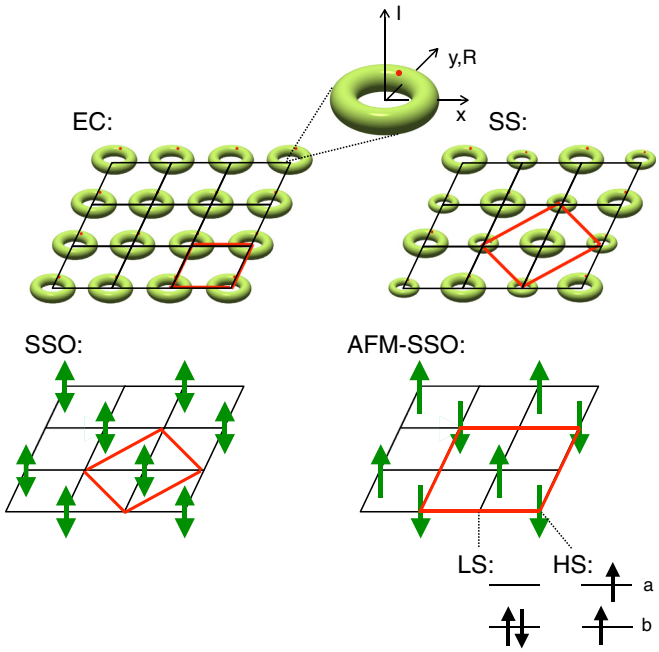

FIG. 1. A cartoon depiction of the ordered phases. The EC order parameter is characterized by (spin) direction in the xy plane and a complex phase and thus lives on the surface of a torus. In the SS phase the EC order parameter has a staggered amplitude. The SSO phase is characterized by alternating HS and LS sites, with fluctuating orientation of the HS moment. In the AFM-SSO phase the HS moments order in AFM superstructure. The primitive period cell in each phase is marked with the red square. The occupation of the atomic a and b orbitals in the LS and one of the HS states is shown in the bottom right corner.

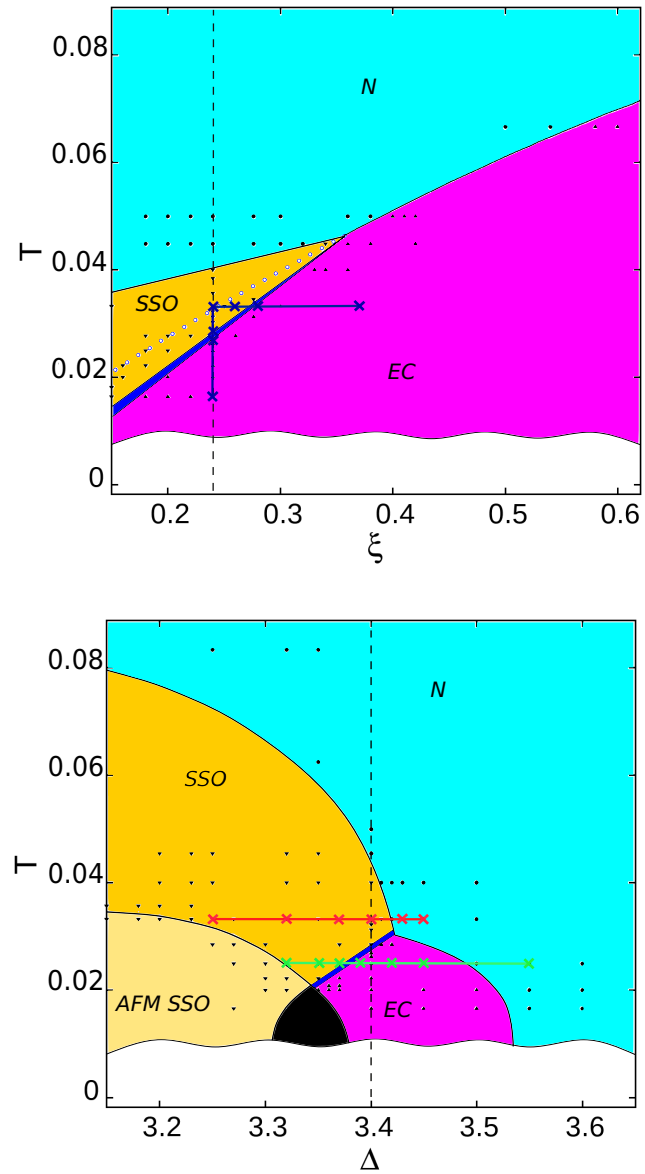

FIG. 2. Cuts through the phase diagram of the studied model along the ξ–T ($\Delta = 3.4$, top) and Δ–T ($\xi = 0.24$, bottom) planes. Black symbols mark the parameters for which a calculation was performed. The dashed vertical line is common to both panels. The narrow blue wedge separating the EC and SSO phases represents the SS phase. The red, blue and violet cuts with crosses mark the points for which the susceptibilities are analyzed in Figs. 5, 6, and 7, respectively. Open blue circles in the left panel were taken from Ref. [21] and indicate instability of the normal (N) phase towards EC. The black wedge separating the AFM-SSO and EC phases in the right panel indicate a putative coexistence regime accompanying a first order transition. (Actual calculations investigating this transition were not performed).

Spin state order. The SSO phase in the two-band Hubbard model was reported in Ref. [32] and in multiorbital material specific DMFT studies [41,42]. It was proposed as an explanation of high field experiments on $LaCoO_3$ [43,44]. It is characterized by staggered orbital polarization $\Delta O = (-1)^i \langle O_i - \bar{O} \rangle$, where $(-1)^i$ describes the $\sqrt{2} \times \sqrt{2}$ order and $\bar{O}$ denotes an average over all lattice sites. The SSO is a strong-coupling effect that, unlike the EC phase, does not have a weak-coupling analog [21]. At $T = 0$ the phase is a checkerboard arrangement of low spin (LS) and high spin (HS) sites. In the studied parameter range the LS-like sites are dominated by the LS state with a negligible HS contribution. The population of the HS state on HS-like sites is only up to 60%, with the remainder being predominantly LS states [45]. The SSO phase breaks the translation symmetry, but the continuous $U(1)$ symmetries associated with S^z and O conservation are preserved.

Supersolid (SS). The SS phase is characterized by the simultaneous appearance of the EC and SSO orders [46,47]. The SS phase breaks all the symmetries broken by EC and SSO phases. We consistently find a very narrow strip of the SS phase at the boundary between the EC and SSO phases, see Fig. 3.

Antiferromagnetic spin state order (AFM-SSO). The SSO phase has a large residual entropy associated with the spin disorder on the HS sites. The nearest neighbor AFM exchange interaction on the HS sublattice (third neighbor interaction on the original lattice) leads to a 2×2 order consisting in checkerboard spin order on the HS sublattice. We did not actually perform calculations in the AFM-SSO phase, but determined the SSO/AFM-SSO phase boundary as the divergence of $\tilde{\chi}^{S^z}(M', 0)$, see Fig. 4.

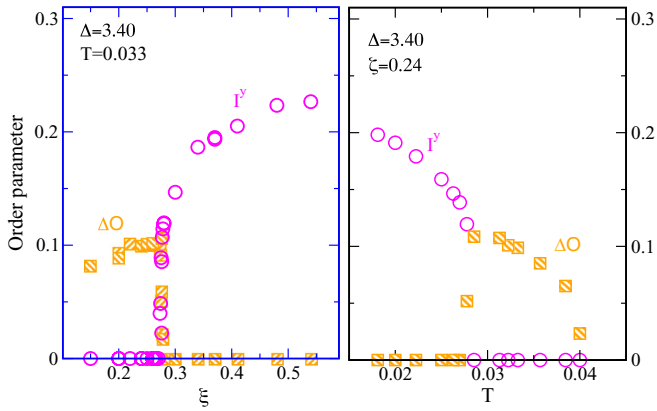

FIG. 3. The order parameters: staggered orbital polarization ΔO and the uniform excitonic-condensate amplitude $\langle I^y \rangle$ along the cuts in the phase diagram Fig. 2 marked by the frame colors.

B. Dynamical susceptibility

The main focus of this work is the behavior of the dynamical susceptibility across the transition between the EC and SSO states. In Fig. 5 we show the evolution of $\chi^X(\mathbf{k}, \omega)$ (X=O, S^z, R^x, I^x, R^y, I^y) along the Γ-X-M-Γ path in the two-dimensional Brillouin zone with increasing crystal fields Δ.

First, we review the discussion of the N–EC transition from Ref. [30]. The normal (N) phase is characterized by gapped excitonic dispersion, reflected in all excitonic susceptibilities. The equivalence of x and y elements originates from the S^z conservation, while the equivalence of R and I elements originates from the O conservation. The O and S^z susceptibilities exhibit no dynamics (non-zero only for $\nu_n = 0$) and vanish at low temperature. Reducing Δ results in closing of the excitonic gap and eventually transition to the EC phase, where the equivalence of excitonic susceptibilities is broken. Deep in the EC phase we can distinguish x and y excitonic modes with distinct dispersion. The corresponding susceptibilities R_x, I_x and R_y, I_y follow these dispersions, but have vastly different amplitudes at low energies. The I^x and R^y exhibit linear dispersion and diverging amplitudes at Γ, reflecting the spin-rotation and phase-rotation Goldstone modes [30].

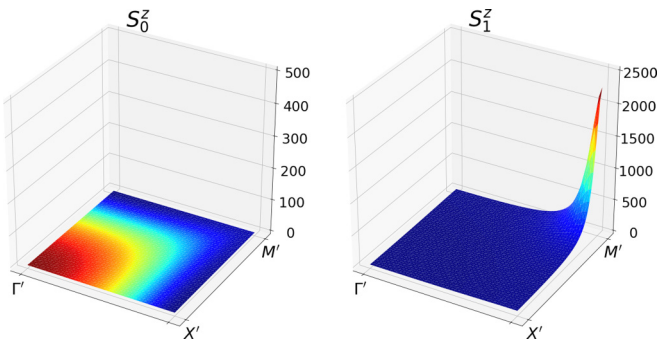

FIG. 4. Site resolved static susceptibility $\chi^{S^z}(\mathbf{k}')$ for $T = 0.0333$, ξ=0.24, Δ =3.23 in the SSO phase. It describes the response to a field applied only on the LS-like sublattice (left) and on the HS-like sublattice (right). The reciprocal vector $\mathbf{k}'$ is expressed with respect to the two-atom unit cell.

The S^z and O susceptibilities acquire nonzero dynamics due to the S^z–R^x and O–I^y coupling in the EC phase. The induced dynamics of S^z was explained in terms of the strong-coupling model in Ref. [30], see also SM [48]. The dynamical response of O can be understood along similar lines. In the strong coupling limit O_i maps onto the number operator of excitons $O_i = d_{ix}^\dagger d_{ix} + d_{iy}^\dagger d_{iy}$. Replacing $d_{iy}^\dagger$ with $i\frac{\phi}{2} + d_{iy}^\dagger$ in the EC phase we find $O_i \sim -\frac{\phi}{2}(d_{iy}^\dagger - d_{iy})$, and thus the correlation function of O follows that of I^y. For a more rigorous derivation see Supplemental Material [48]. We point out that all the above identifications are understood relative to the orientation of the EC order parameter: $\langle I^y \rangle \neq 0$.

As we near the SSO phase the behavior of the O, S_z, and I_y susceptibilities changes qualitatively. The O and S_z dynamics cease to be slave to the excitonic dynamics and their dispersions stop to follow the excitonic ones. Similar behavior is observed as we approach the phase boundary as a function of crystal field Δ, Fig. 5, band asymmetry ξ or temperature T, Fig. 6. The O susceptibility develops a hot spot at the M point, a precursor of the SSO phase, which is accompanied by softening of χ_y^I at M. Similar behavior at the M point was previously observed at zero temperature for spinless hard-core bosons on square lattice and interpreted as roton excitations known from superfluid helium [47]. We provide the strong-coupling mean-field analysis of the softening and EC–SSO transition in the Supplemental Material [48].

The demise of the EC phase due to the softening of the excitonic mode accompanied by the divergence of $\chi^O(\mathbf{k} = M, 0)$ opens the possibility for a continuous transition between the EC and SSO phases via an intermediate SS phase. Indeed, we find several solutions with both EC and SSO order, Fig. 3, which fall into an narrow strip of parameters. We point out that a similar situation was found in Ref. [47].

In the SSO phase, we observe the remains of broad excitonic dispersion in the vicinity of the phase boundary. It is important to point out that at the studied temperatures, the LS sites host almost exclusively the LS state, but the HS sites host still up to 75% LS and only 25% HS states [32]. Proceeding deeper into the SSO phase the excitonic dispersion gives way to two almost flat bands. These can be associated with creation of an exciton (LS to HS transition) on the LS site (upper band) and annihilation of an exciton (HS to LS transition) on the HS site (lower band).

In Fig. 7 we show the evolution of the excitonic susceptibility [49] across the transition between normal and SSO phase. The exciton dispersion is well pronounced and qualitatively similar in the vicinity of the phase boundary on both sides. The effect of unit cell doubling in the SSO phase on the excitonic dispersion is revealed by the mode analysis discussed below.

C. Mode analysis

The connection between dynamical susceptibilities in Figs. 5, 6, and 7 on the one hand, and bosonic dispersions obtained in the strong coupling model [15,47,48] on the other hand, is not straightforward. In the strong-coupling limit and at $T = 0$, the susceptibilities follow the dispersions of the d_x or d_y bosons with intensity depending on the specific correlation function. Our model is not in the strong-coupling limit and partly falls into a high temperature regime. The

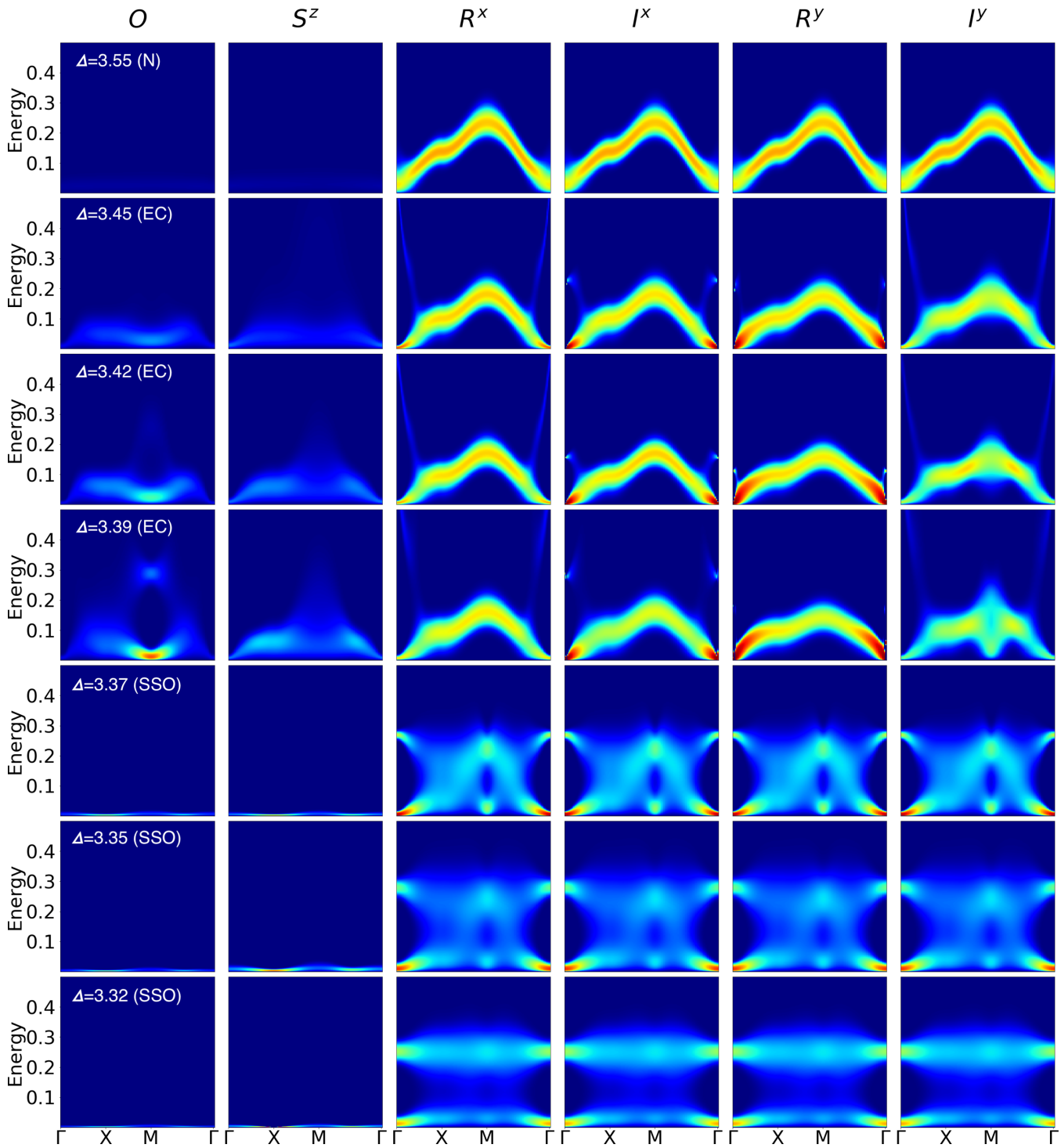

FIG. 5. Evolution of the dynamical susceptibility $\chi^X(\mathbf{k}, \omega)$ with the crystal field Δ along the green line ($\xi = 0.24$, $T = 0.025$) in Fig. 2(b). The columns correspond to different Hermitean operators $X = O, S^z, R^x, I^x, R^y, I^y$. The color coding represents the spectral density $B(\mathbf{k}, \omega) = -\frac{1}{\pi}\,\mathrm{Im}\,\chi^X(\mathbf{k}, \omega)$. In order to capture the entire dispersion in the presence of divergent density of the Goldstone modes we introduce a cutoff and plot $\frac{B}{B+\mathrm{const}}$ with const $= 5.5$. Note that in the SSO phase there is a large intensity of χ^{S^z} at $\omega \approx 0$ (difficult to see in the present figures) corresponding to large static response of local moments on HS sites.

bosonic modes, a 2P basis in which $\boldsymbol{\chi}(\mathbf{k}, \omega)$ is diagonal [50], are not immediately obvious.

We attempt to obtain approximate modes by diagonalizing the static susceptibility $\boldsymbol{\chi}(\mathbf{k}, \omega = 0)$. This procedure is trivial in the normal phase, because each of the four mutually equal excitonic susceptibilities forms a diagonal block of $\boldsymbol{\chi}(\mathbf{k}, \omega)$. In the SSO phase the excitonic susceptibilities do not mix with other elements of $\boldsymbol{\chi}(\mathbf{k}, \omega)$ or with each other, and the diagonalization is reduced to 2×2 blocks spanned by the two sites of the two-atom unit cell.

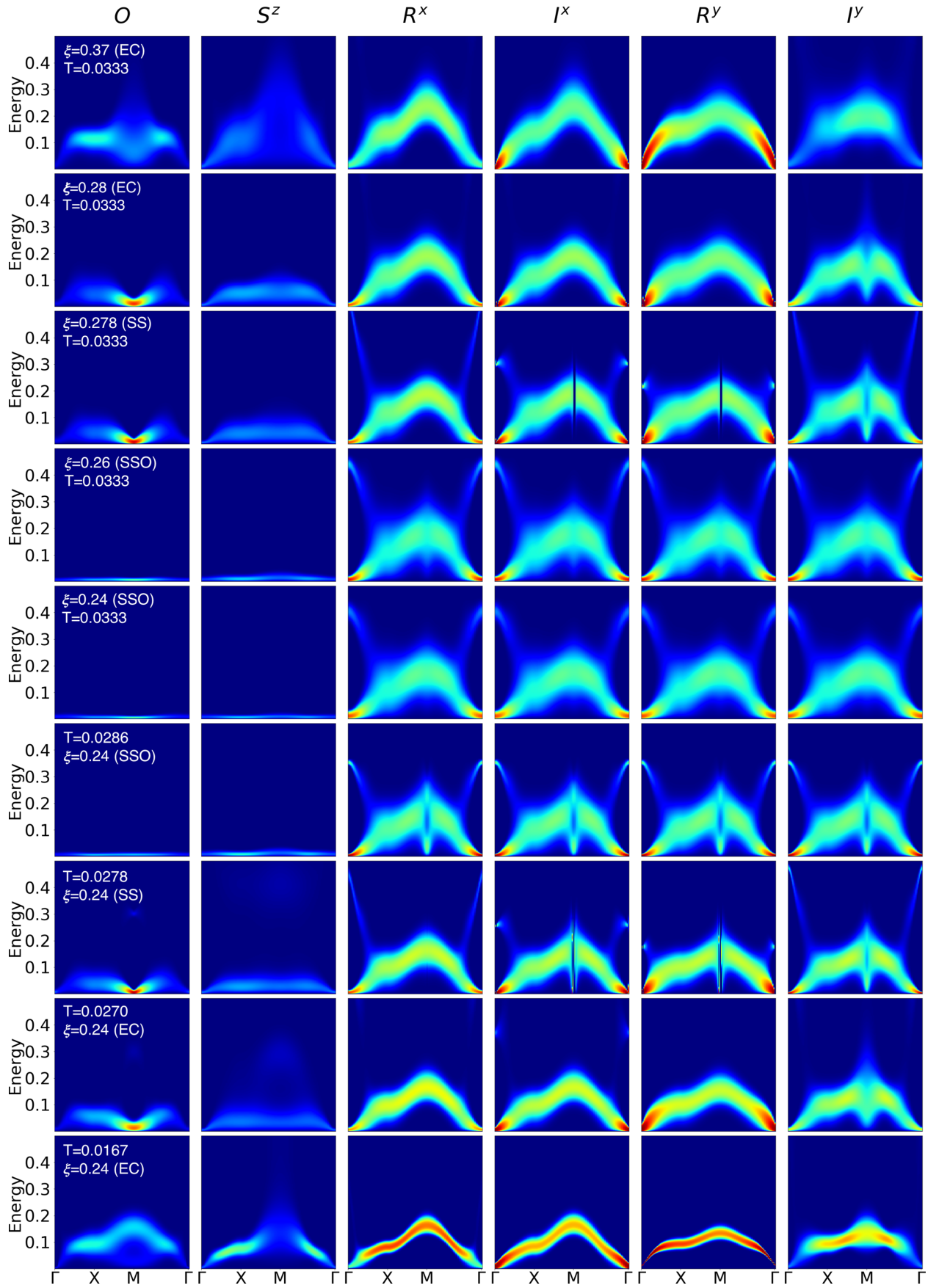

FIG. 6. As in Fig. 5, evolution of the dynamical susceptibility $\chi^X(\mathbf{k}, \omega)$ ($X = O, S^z, R^x, I^x, R^y, I^y$) along the inverted L-shaped blue line in Fig. 2(a) for $\Delta = 3.4$.

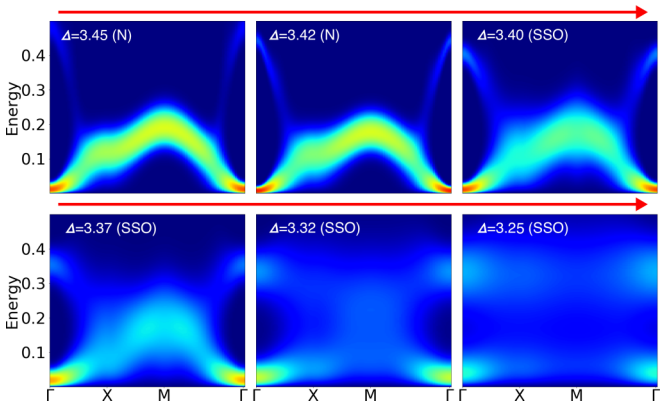

FIG. 7. Evolution of the dynamical excitonic susceptibility $\chi^X(\mathbf{k},\omega)$ with crystal field Δ along the red line(ξ=0.24, T = 0.0333) in Fig. 2(b).

The dominant effect of diagonalization in the EC phase is to combine I^y with O into a single low-energy mode with large spectral weight $\tilde{I}^y$. In Fig. 8, we show the evolution of $\chi^{\tilde{I}^y}(\mathbf{k},\omega)$ as we approach the EC/SS phase boundary by varying the temperature along the cut analyzed in Fig. 6. Deep in the EC phase, $\chi^{\tilde{I}^y}$ is essentially identical to χ^{I^y}. As we get closer to the phase boundary, a mode softening at the M point is clearly observable. Interestingly, it does not proceed as a smooth deformation of the dispersion curve captured by the strong-coupling model [48], but rather through a spectral weight transfer between the upper and low branch of the O-ring structure observed at T= 0.025. It is unclear whether this deviation from the spin-wave treatment of the strong-coupling model [15] originates from the finite temperature or the departure for the strong-coupling limit.

In Figs. 9 and 10, we show the mode decomposition in the SSO phase. For all parameters we find two bands reminiscent of the strong-coupling behavior [15,47]. Deep in the SSO phase the bands are flat. The lower one corresponds to eliminating a HS exciton on the nominally HS sublattice. The upper band corresponds to creating a HS exciton on the nominally LS sublattice. With increasing crystal field Δ, the character of the bands changes and they become dispersive, while the gap

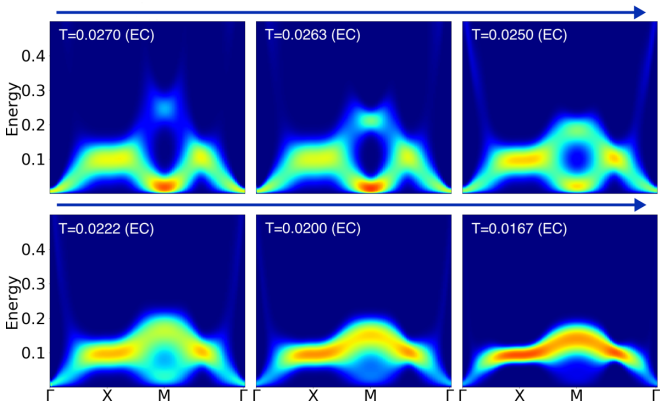

FIG. 8. Dynamical susceptibility $\chi^{\tilde{I}^y}(\mathbf{k},\omega)$ in the EC phase of Fig. 6 (vertical part of the L-shaped cut; $\Delta = 3.40$, $\xi = 0.24$) in the basis of the eigenmodes of the static susceptibility.

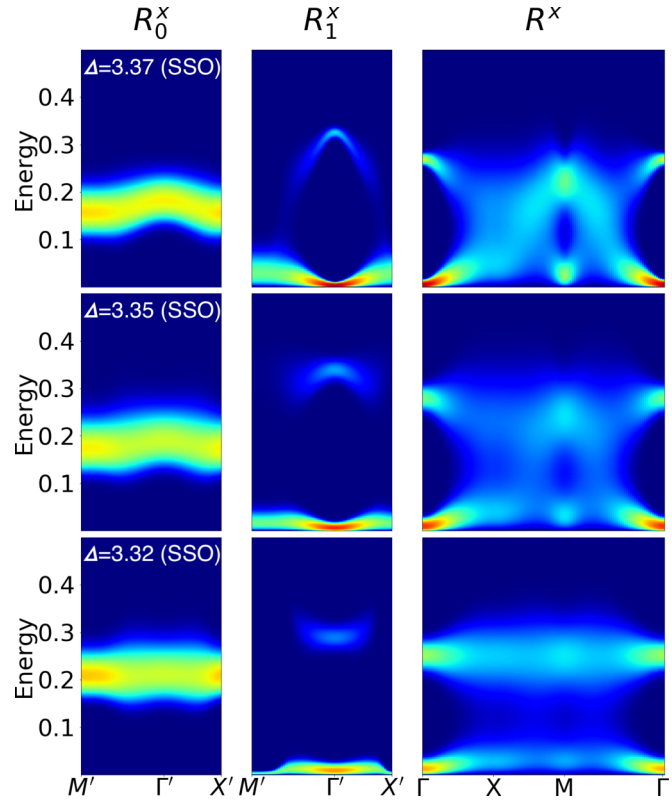

FIG. 9. Dynamical excitonic susceptibilities $\chi^X(\mathbf{k},\omega)$ in the SSO phase of Fig. 5 ($T = 0.025$) in the basis of the eigenmodes of the static susceptibility. The R_0^x and R_1^x columns refer to the two eigenmodes (of the static susceptibility) in the two-atom unit cell. The k path refers to the Brillouin zone for the two-atom unit cell. The R^x column reproduces the data from Fig. 5 for comparison (k path in the Brillouin zone of one-atom unit cell). Note that in the SSO all excitonic susceptibilities are identical and R^x was chosen as their representative.

between them shrinks. This behavior is somewhat counterintuitive, since the difference of HS and LS energies in an isolated atom follows an opposite trend. The explanation lies with the nearest-neighbor repulsion between HS excitons. Increasing Δ causes a decrease in concentration of HS states on the nominally HS sublattice, which reduces the HS-HS repulsion that has to be overcome when creating a HS exciton on the nominally LS sublattice. Simultaneously, a minute shift of the lower excitonic band leads to a condensation as the SSO/SS boundary is approached. At the SSO/N boundary, Fig. 10, the temperature is too high for the excitons to condense. We observe a complete closing of the gap between the two bands, which become a back-folded image of the excitonic band from the one-atom unit cell. In addition to the two main bands, we observe a weak high-energy feature around the Γ' point, which does not have a strong-coupling $T = 0$ counterpart. This feature exhibits a rather strong dispersion and it is most pronounced close to the boundary of SSO with either the SS or normal phases, Figs. 9 and 10 [51].

The phase diagram of the two-band Hubbard model is extremely rich and we have addressed its small part, relevant for insulators (or metals close to Mott transition) in the vicinity of spin-state transition [18] such as the perovskite cobaltites.

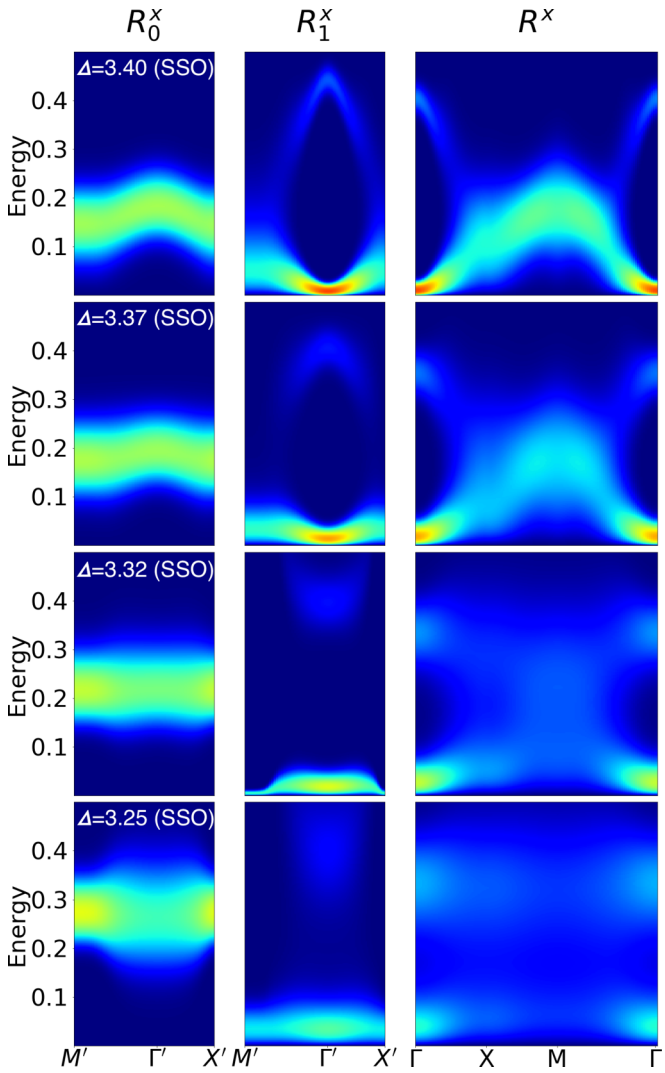

FIG. 10. Dynamical excitonic susceptibilities $\chi^X(\mathbf{k},\omega)$ in the SSO phase of Fig. 7 ($T = 0.0333$) in the basis of the eigenmodes of the static susceptibility. The notation is the same as in Fig. 9.

While the excitonic instability can be found in the insulator as well as in the weakly coupled metal [12], the spin-state ordering is a strong coupling effect [21] found in an insulator or strongly correlated metal. Our preliminary calculations with asymmetric bands as well as the study of Ref. [12] for symmetric bands show that deep in the metallic phase the SSO instability is absent and the excitonic condensation competes with antiferromagnetism. The role of the Hund's J in the present model built on two-orbital atoms is twofold, it determines the interorbital interaction U' and the spin state of the lowest atomic excitation. If these roles can be separated, for example, by considering a and b to label the layers of a bilayer system and $U' + \Delta \approx U$, the competition between EC and SSO phases can take place even for $J \leqslant 0$ [52,53], although the detailed nature of these phases differs from the present case.

IV. CONCLUSIONS

We have studied the dynamical susceptibility across several phase transitions in the two-orbital Hubbard model using DMFT. We have observed a narrow slip of supersolid phase separating the spin-state order from the excitonic condensate. Approaching the spin-state ordered phase from the exciton condensate is heralded by the softening of a specific collective mode at the M point of the Brillouin zone, identified as the roton instability in Ref. [47]. At low temperatures the spin-state ordered phase removes the spin degeneracy by developing antiferromagnetic order with 2×2 periodicity.

The present calculations demonstrate the utility of linear response DMFT formalism for understanding complicated phase diagrams and phase transitions involving the breaking of both discrete and continuous symmetries. While the DMFT susceptibilities in the studied parameter range qualitatively agree with the strong-coupling generalized spin-wave treatment [15,47,48], they contain features that are beyond this description. Last but not least, we have shown that the symmetry breaking in the exciton condensate gives rise to dynamical response in the spin- and orbital-density channels. These may be studied by standard experimental probes such as inelastic x-ray or neutron scattering, which do not couple directly to the spin-triplet excitonic channel.

ACKNOWLEDGMENTS

The authors thank A. Kauch and R. T. Scalettar for comments and critical reading of the manuscript. This work was supported by the European Research Council (ERC) under the European Union's Horizon 2020 research and innovation programme (Grant agreement No. 646807-EXMAG). The authors acknowledge support by the Czech Ministry of Education, Youth and Sports from the Large Infrastructures for Research, Experimental Development and Innovations project IT4Innovations National Supercomputing Center LM2015070. The calculations were performed at Vienna Scientific Cluster.

[1] N. F. Mott, Philos. Mag. **6**, 287 (1961).
[2] L. V. Keldysh and Y. V. Kopaev, Sov. Phys. Solid State **6**, 2219 (1965).
[3] B. I. Halperin and T. M. Rice, *Solid State Physics* (Academic Press, New York, 1968), p. 115.
[4] J. P. Eisenstein and A. H. MacDonald, Nature (London) **432**, 691 (2004).
[5] R. Balili, V. Hartwell, D. Snoke, L. Pfeiffer, and K. West, Science **316**, 1007 (2007).
[6] H. Cercellier, C. Monney, F. Clerc, C. Battaglia, L. Despont, M. G. Garnier, H. Beck, P. Aebi, L. Patthey, H. Berger, and L. Forró, Phys. Rev. Lett. **99**, 146403 (2007).
[7] A. Kogar, M. S. Rak, S. Vig, A. A. Husain, F. Flicker, Y. I. Joe, L. Venema, G. J. MacDougall, T. C. Chiang, E. Fradkin, J. van Wezel, and P. Abbamonte, Science **358**, 1314 (2017).
[8] A. Jain, M. Krautloher, J. Porras, G. H. Ryu, D. P. Chen, D. L. Abernathy, J. T. Park, A. Ivanov, J. Chaloupka, G. Khaliullin, B. Keimer, and B. J. Kim, Nat. Phys. **13**, 633 (2017).

[9] S. Tsubouchi, T. Kyômen, M. Itoh, P. Ganguly, M. Oguni, Y. Shimojo, Y. Morii, and Y. Ishii, Phys. Rev. B **66**, 052418 (2002).

[10] T. Moyoshi, K. Kamazawa, M. Matsuda, and M. Sato, Phys. Rev. B **98**, 205105 (2018).

[11] J. Kuneš and P. Augustinský, Phys. Rev. B **90**, 235112 (2014).

[12] S. Hoshino and P. Werner, Phys. Rev. B **93**, 155161 (2016).

[13] T. Kaneko and Y. Ohta, Phys. Rev. B **90**, 245144 (2014).

[14] G. Khaliullin, Phys. Rev. Lett. **111**, 197201 (2013).

[15] J. Nasu, T. Watanabe, M. Naka, and S. Ishihara, Phys. Rev. B **93**, 205136 (2016).

[16] T. Tatsuno, E. Mizoguchi, J. Nasu, M. Naka, and S. Ishihara, J. Phys. Soc. Jpn. **85**, 83706 (2016).

[17] J. Kuneš, J. Phys. Condens. Matter **27**, 333201 (2015).

[18] P. Werner and A. J. Millis, Phys. Rev. Lett. **99**, 126405 (2007).

[19] A. Georges, G. Kotliar, W. Krauth, and M. Rozenberg, Rev. Mod. Phys. **68**, 13 (1996).

[20] G. Kotliar, S. Y. Savrasov, K. Haule, V. S. Oudovenko, O. Parcollet, and C. A. Marianetti, Rev. Mod. Phys. **78**, 865 (2006).

[21] J. Kuneš and P. Augustinský, Phys. Rev. B **89**, 115134 (2014).

[22] J. Kuneš and V. Křápek, Phys. Rev. Lett. **106**, 256401 (2011).

[23] A. Georges and G. Kotliar, Phys. Rev. B **45**, 6479 (1992).

[24] M. Jarrell, Phys. Rev. Lett. **69**, 168 (1992).

[25] B. Bauer, L. D. Carr, H. G. Evertz, A. Feiguin, J. Freire, S. Fuchs, L. Gamper, J. Gukelberger, E. Gull, S. Guertler, A. Hehn, R. Igarashi, S. V. Isakov, D. Koop, P. N. Ma, P. Mates, H. Matsuo, O. Parcollet, G. Pawłowski, J. D. Picon, L. Pollet, E. Santos, V. W. Scarola, U. Schollwöck, C. Silva, B. Surer, S. Todo, S. Trebst, M. Troyer, M. L. Wall, P. Werner, and S. Wessel, J. Stat. Mech.: Theory Exp. (2011) P05001.

[26] H. Shinaoka, E. Gull, and P. Werner, Comput. Phys. Commun. **215**, 128 (2017).

[27] A. Gaenko, A. E. Antipov, G. Carcassi, T. Chen, X. Chen, Q. Dong, L. Gamper, J. Gukelberger, R. Igarashi, S. Iskakov, M. Könz, J. P. LeBlanc, R. Levy, P. N. Ma, J. E. Paki, H. Shinaoka, S. Todo, M. Troyer, and E. Gull, Comput. Phys. Commun. **213**, 235 (2017).

[28] P. Werner, A. Comanac, L. de' Medici, M. Troyer, and A. J. Millis, Phys. Rev. Lett. **97**, 076405 (2006).

[29] J. E. Gubernatis, M. Jarrell, R. N. Silver, and D. S. Sivia, Phys. Rev. B **44**, 6011 (1991).

[30] D. Geffroy, J. Kaufmann, A. Hariki, P. Gunacker, A. Hausoel, and J. Kuneš, Phys. Rev. Lett. **122**, 127601 (2019).

[31] L. Boehnke, H. Hafermann, M. Ferrero, F. Lechermann, and O. Parcollet, Phys. Rev. B **84**, 075145 (2011).

[32] J. Kuneš, Phys. Rev. B **83**, 085102 (2011).

[33] E. G. C. P. van Loon, H. Hafermann, A. I. Lichtenstein, and M. I. Katsnelson, Phys. Rev. B **92**, 085106 (2015).

[34] F. Krien, E. G. C. P. van Loon, H. Hafermann, J. Otsuki, M. I. Katsnelson, and A. I. Lichtenstein, Phys. Rev. B **96**, 075155 (2017).

[35] J. Otsuki, M. Ohzeki, H. Shinaoka, and K. Yoshimi, Phys. Rev. E **95**, 061302(R) (2017).

[36] H. Shinaoka, D. Geffroy, M. Wallerberger, J. Otsuki, K. Yoshimi, E. Gull, and J. Kuneš, Sci. Post. Phys. **8**, 012 (2020).

[37] J. Kuneš, Phys. Rev. B **90**, 235140 (2014).

[38] J. Kuneš and D. Geffroy, Phys. Rev. Lett. **116**, 256403 (2016).

[39] D. Geffroy, A. Hariki, and J. Kuneš, Phys. Rev. B **97**, 155114 (2018).

[40] L. Balents, Phys. Rev. B **62**, 2346 (2000).

[41] M. Karolak, M. Izquierdo, S. L. Molodtsov, and A. I. Lichtenstein, Phys. Rev. Lett. **115**, 046401 (2015).

[42] J. F. Afonso, A. Sotnikov, A. Hariki, and J. Kuneš, Phys. Rev. B **99**, 205118 (2019).

[43] M. M. Altarawneh, G.-W. Chern, N. Harrison, C. D. Batista, A. Uchida, M. Jaime, D. G. Rickel, S. A. Crooker, C. H. Mielke, J. B. Betts, J. F. Mitchell, and M. J. R. Hoch, Phys. Rev. Lett. **109**, 037201 (2012).

[44] A. Ikeda, T. Nomura, Y. H. Matsuda, A. Matsuo, K. Kindo, and K. Sato, Phys. Rev. B **93**, 220401(R) (2016).

[45] By occupation we mean the diagonal elements of the site-reduced density matrix operator.

[46] M. Boninsegni and N. V. Prokof'ev, Rev. Mod. Phys. **84**, 759 (2012).

[47] R. T. Scalettar, G. G. Batrouni, A. P. Kampf, and G. T. Zimanyi, Phys. Rev. B **51**, 8467 (1995).

[48] See Supplemental Material at http://link.aps.org/supplemental/10.1103/PhysRevB.102.085159 for details about the strong coupling treatment of the model.

[49] Note that both in the normal and SSO phases all the excitonic susceptibilities are equal.

[50] Unless symmetry is enforced, the diagonal character can be only approximate as it is not possible to diagonalize $\boldsymbol{\chi}(\mathbf{k}, \omega)$ for all bosonic frequencies simultaneously.

[51] Note that there is a minor mismatch between the energy of this feature obtained in the second and third column of these figures. We attribute this to analytic continuation procedure, which is performed for the different bases independently and may have difficulty with accurate positioning of small high-energy peak in the spectrum containing large low-energy peak.

[52] L. Rademaker, J. van den Brink, H. Hilgenkamp, and J. Zaanen, Phys. Rev. B **88**, 121101(R) (2013).

[53] L. Rademaker, J. van den Brink, J. Zaanen, and H. Hilgenkamp, Phys. Rev. B **88**, 235127 (2013).